Supporting Information

Enhanced Hydrogen Evolution Reaction Performance of Anatase-Rutile TiO₂ Heterojunction via Charge Transfer from Rutile to Anatase

Nurul Affiqah Arzaee[a,b], Nuttapon Yodsin[c], Habib Ullah[d*], Sabiha Sultana[d,e], Mohamad Firdaus Mohamad Noh[a,b], Ahmad Wafi Mahmood Zuhdi[b], Abd Rashid Bin Mohd Yusoff[f], Siriporn Jungsuttiwong[c*], Mohd Asri Mat Teridi[a*]

[a]Solar Energy Research Institute, Universiti Kebangsaan Malaysia, 43600 Bangi, Selangor, Malaysia.

[b]Institute of Sustainable Energy (ISE), Universiti Tenaga Nasional (UNITEN), Jalan IKRAM-UNITEN, 43000 Kajang, Selangor, Malaysia.

[c]Center for Organic Electronics and Alternative Energy, Department of Chemistry and Center for Innovation in Chemistry, Faculty of Science, Ubon Ratchathani University, Ubon Ratchathani 34190, Thailand.

[d]Department of Engineering, Faculty of Environment, Science and Economy, University of Exeter, Penryn Campus, Cornwall TR10 9FE, United Kingdom

[e]Department of Chemistry, Islamia College Peshawar, Khyber Pakhtunkhwa, 25120, Pakistan

[f]Department of Chemical Engineering, Pohang University of Science and Technology (POSTECH), 77 Cheongam-Ro, Nam-Gu, Pohang 37673, Republic of Korea.

*Corresponding author: asri@ukm.edu.my (M.A.M. Teridi) Phone: +603 8911 8580

*Corresponding author: siriporn.j@ubu.ac.th (S. Jungsuttiwong) Phone: +66 8 1692 4610

*Corresponding author: hu203@exeter.ac.uk (H. Ullah)
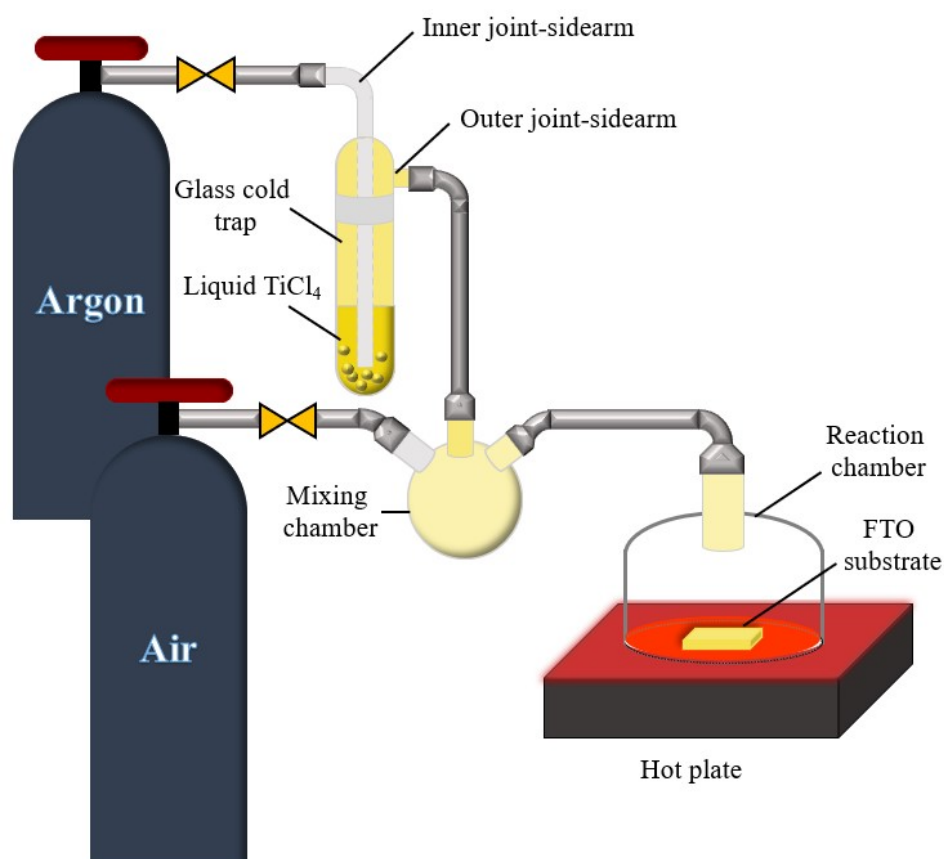
Fig. S1 Schematic diagram of the APCVD system for the fabrication of TiO$_2$ photoanode.

TiO$_2$ thin films were prepared using a custom-built vertical APCVD system as illustrated in Fig. S1. Generally, the system consists of three main interconnected parts including precursor supply unit, mixing and reaction chambers. In the precursor supply unit, TiCl$_4$ precursor vapor was transported using argon gas into the mixing chamber, where it mixed with purified air that acts as oxygen source. The precursor mixture then flowed into the reaction chamber, in which thermal decomposition of the precursor occurred, leading to the formation of TiO$_2$ layer on the FTO substrate. Deposition conditions were then optimized in order to obtain high-performance TiO$_2$ photoanode. It is found that the effective modulation of crystal phase, crystallographic defect and morphology of photoanode can lead to significant improvement in PEC performance
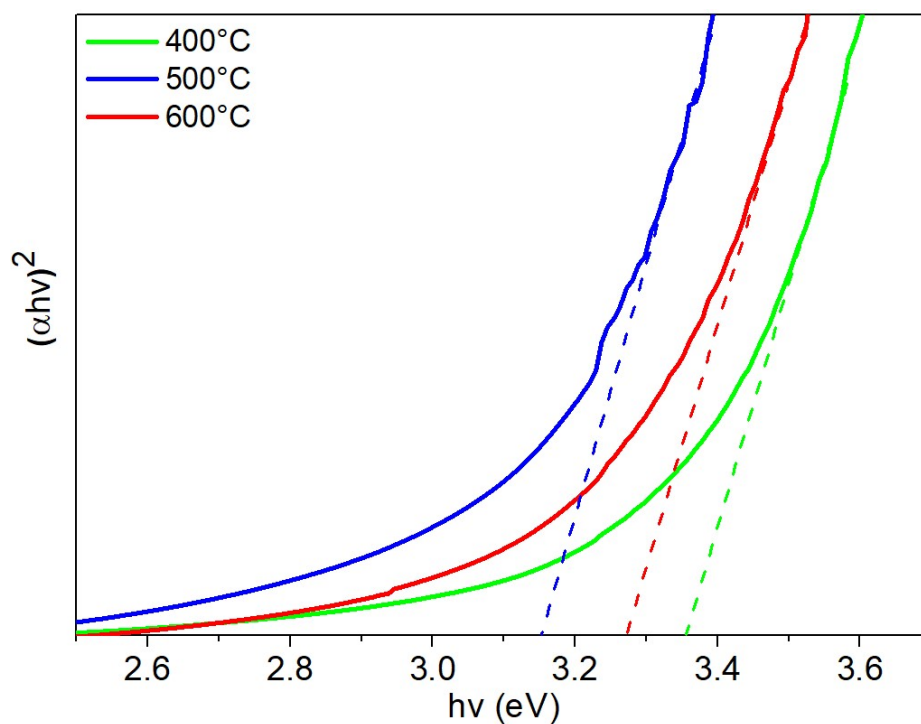
Fig. S2 Tauc plot of TiO$_2$ thin film synthesized at 400, 500 and 600ºC.
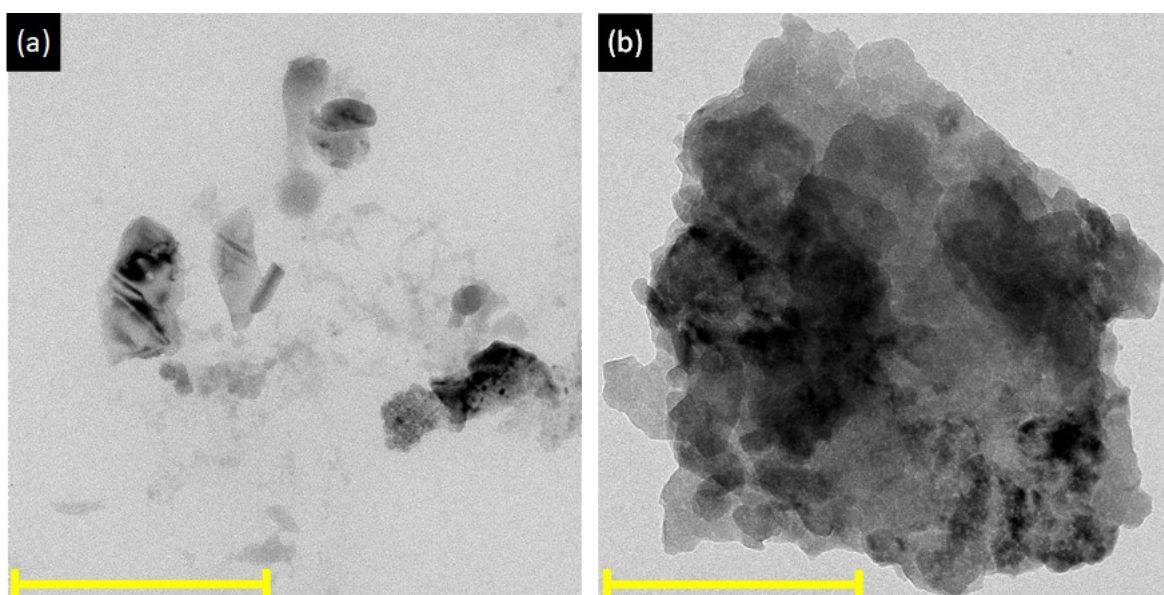
Fig. S3 TEM images showing (a) nanoparticle and (b) nanoflake fragments of TiO$_2$ deposited at 500 °C (scale bar represents 200 nm). The scratching and ultrasonic dispersion techniques were used in the preparation of TiO$_2$ sample for TEM analysis, which caused the structures to collapse into small fragments.
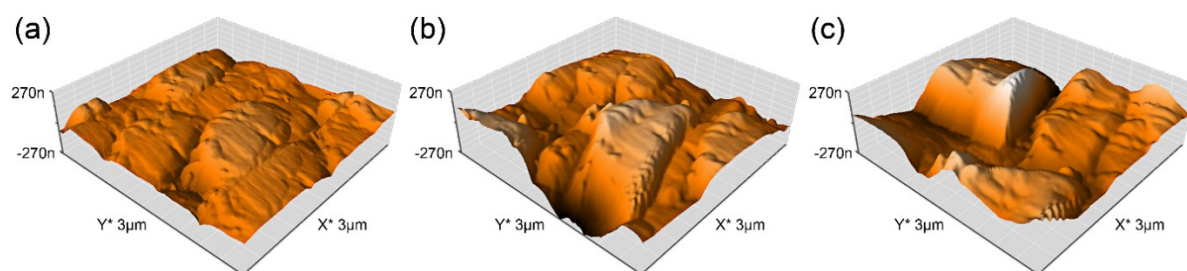
Fig. S4 3-dimensional views from AFM images of TiO$_2$ film deposited at (a) 400ºC, (b) 500ºC and (c) 600ºC.
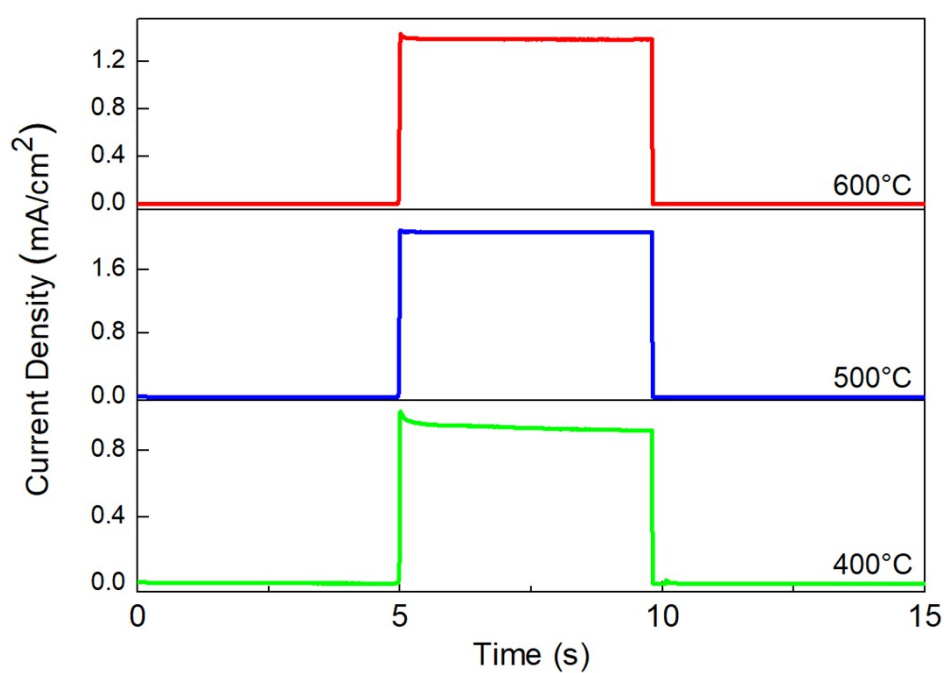
Fig. S5 Zoom-in view of the chronoamperometric scans of TiO$_2$ deposited at different temperatures under chopped illumination measured at bias voltage of 1.23 V$_{RHE}$.
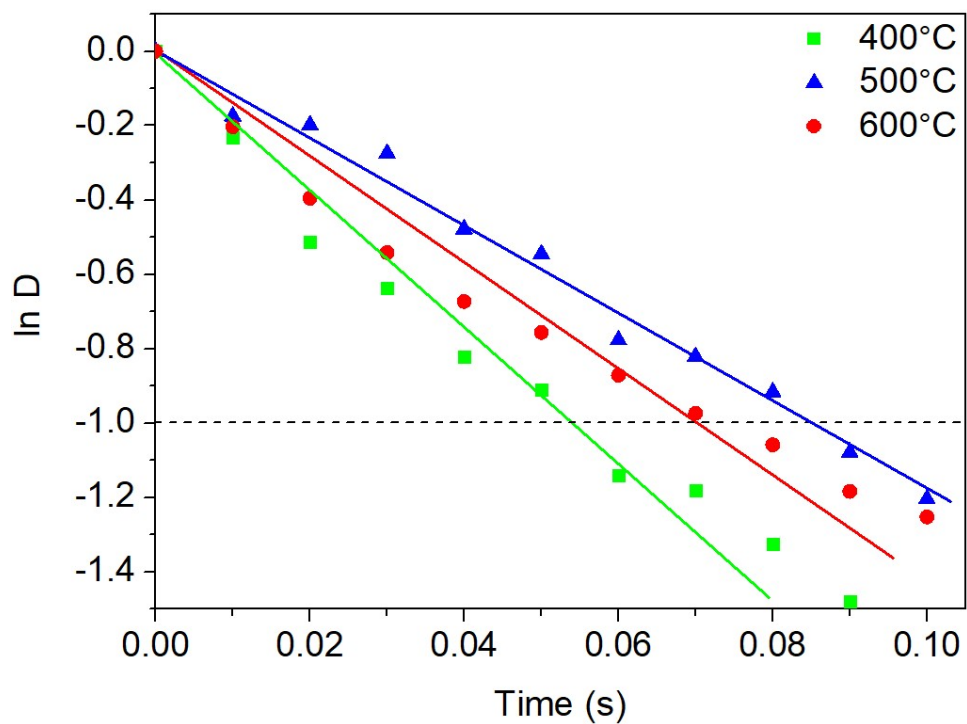
Fig. S6 ln *D* vs. time curves for the determination of transient time calculated from chronoamperometric scans.
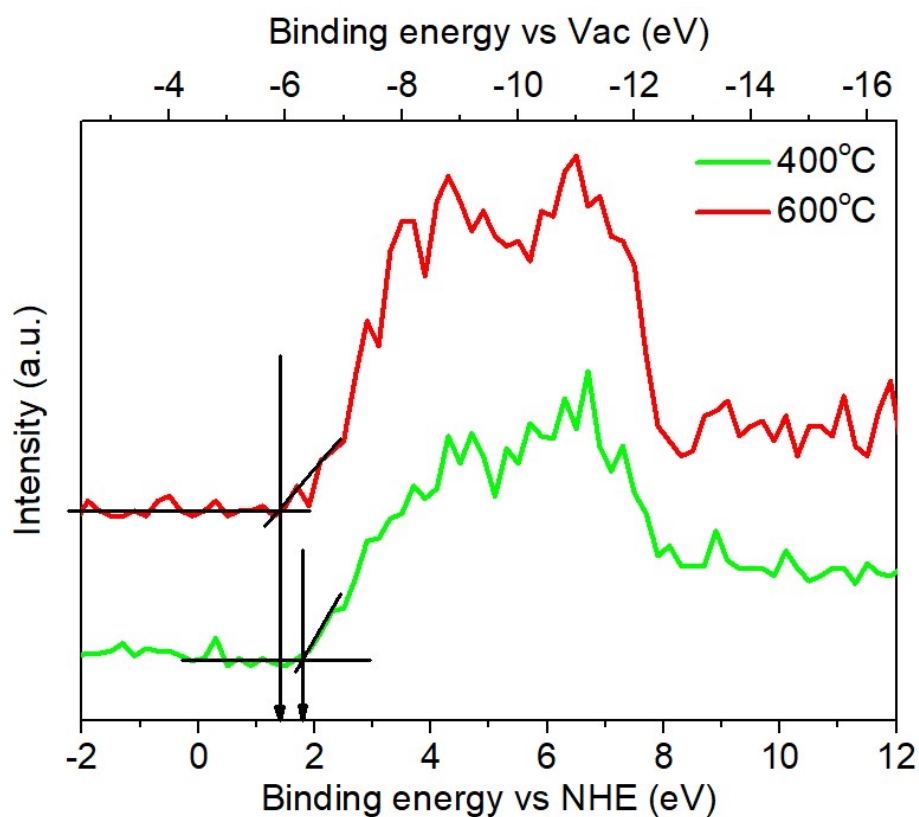
Fig. S7 XPS valence band of TiO_2 deposited at 400°C and 600°C for assisting in the construction of energy band alignment.

In this work, the electronic structure is constructed using the equation $E_{CB} = E_{VB}-E_g$, where E_{CB} is the conduction band, E_{VB} is the valence band determined from XPS valence band (Fig. S5) and E_g is the band gap determined from Tauc plot (Fig. S1). TiO_2-400 is selected as the representative sample for pure anatase. On the other hand, the exact values of E_{VB} and E_{CB} of the rutile TiO_2 cannot be determined due to mixture of both phases in the TiO_2-500 and TiO_2-600 samples. Hence, TiO_2-600, which has high rutile content, is chosen to see the effect of rutile phase on the electronic structure. The E_{VB} of pure anatase TiO_2-400 is -6.3 eV_{Vac} whereas the E_{VB} shifts to -5.9 eV_{Vac} for mixed-phase TiO_2-600. The E_g of TiO_2-400 and TiO_2-600 estimated from Tauc plot are 3.36 eV and 3.28 eV, respectively. Therefore, the corresponding E_{CB} position of TiO_2-400 and TiO_2-600 are at -2.94 eV_{Vac} and –2.62 eV_{Vac}. From these values, it is postulated that the conduction and valence bands of rutile TiO_2 is higher than that of

anatase TiO$_2$. The shift of the electronic structure to the higher position is supported by the Mott-Schottky analysis. It is known that the x-intercepts of Mott-Schottky plot reflects the flat band potential (E$_{FB}$). For n-type TiO$_2$, the E$_{fb}$ is close to the E$_{CB}$ of the material. The E$_{FB}$ for the TiO$_2$ deposited at 500 and 600°C shift slightly to more negative potential (vs. RHE) with respect to 400°C-based photoanode. The shifting of flat band potential is caused by the emergence of rutile phase in both samples, signifying the higher position of conduction band of rutile than that of anatase. Both XPS and Mott-Schottky measurements confirm that the electronic structure of rutile phase is higher than that of anatase phase as illustrated in Fig. 4a.
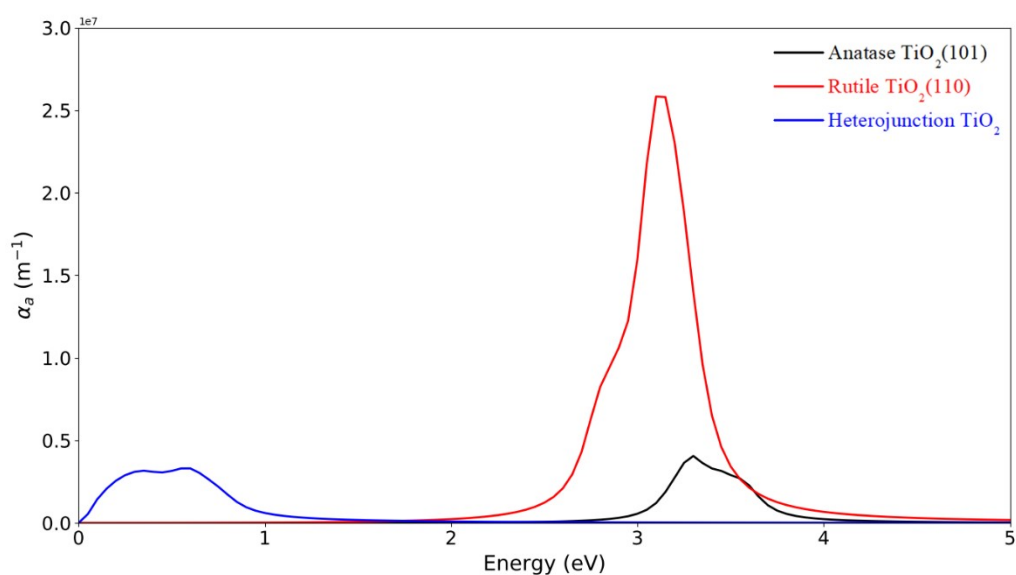
Fig. S8 Comparative optical spectra of Anatase, Rutile and Heterojunction TiO$_2$.
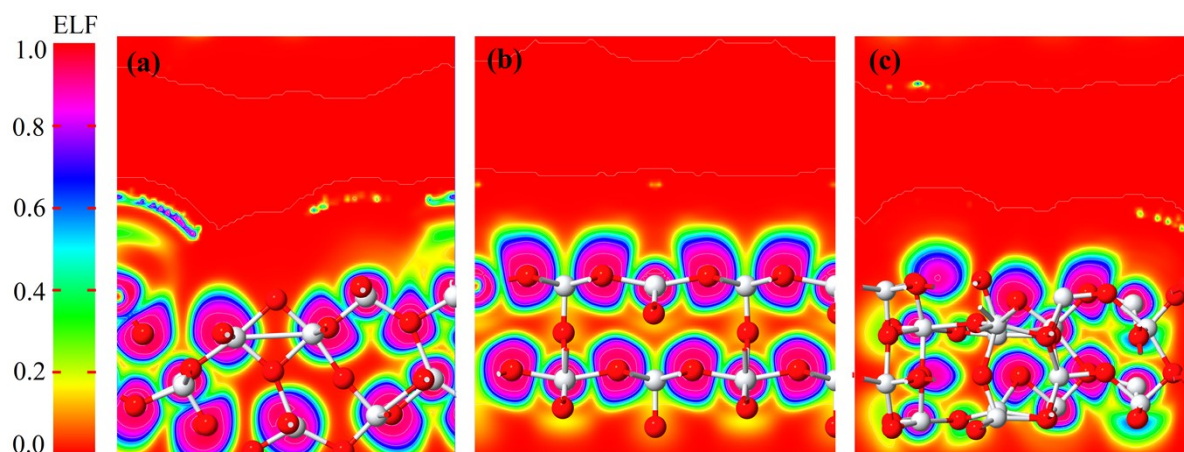
Fig. S9 Electron Localization Function of Anatase (a), Rutile (b) and Heterojunction TiO_2 (c).
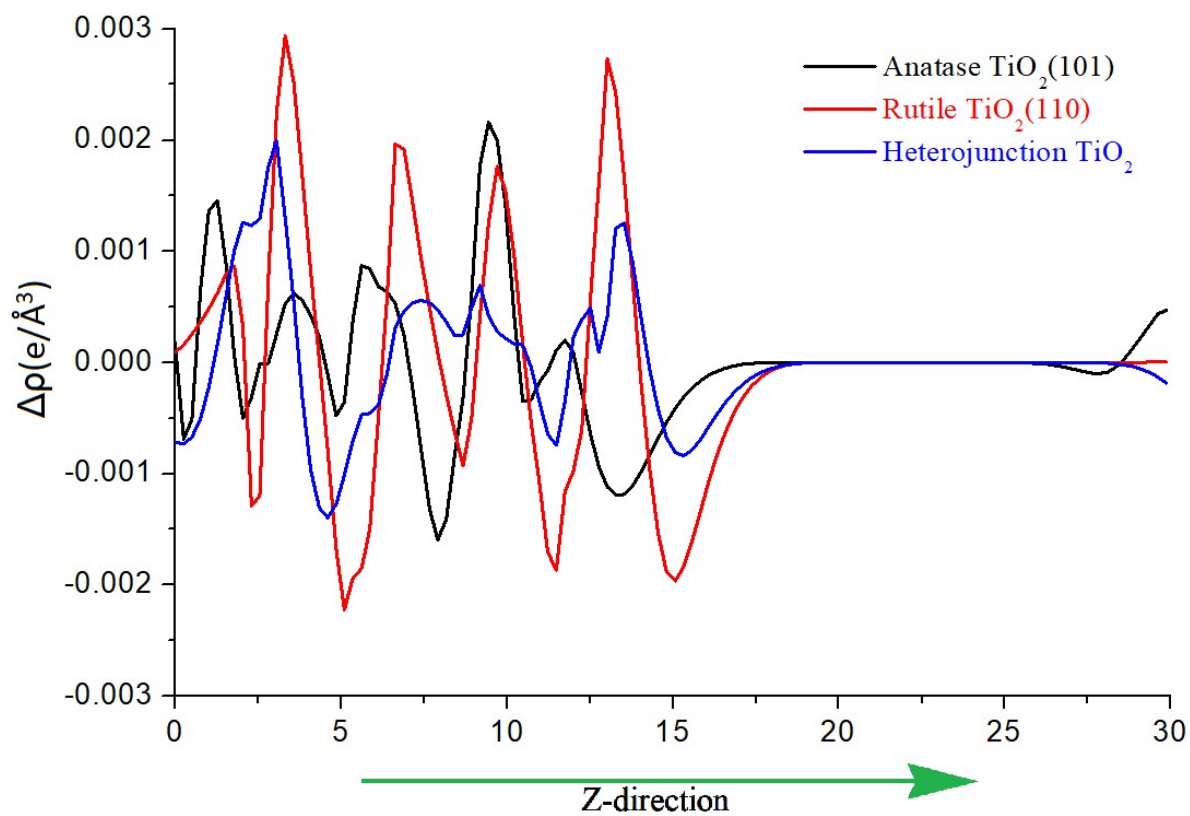
Fig. S10 2D plot of the EDD of Anatase, Rutile, and Heterojunction TiO_2 along Z-direction.
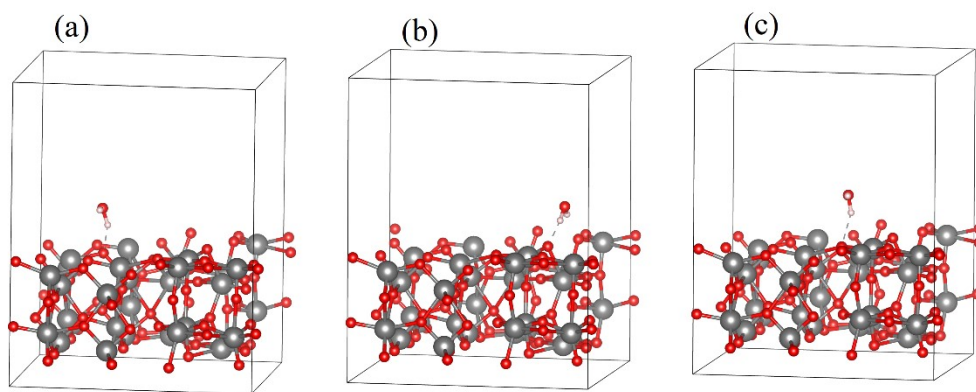
Fig. S11 Optimized geometric structure of Anatase/Rutile Heterojunctions, where one water molecule is interacted at Anatase (a), Rutile (b), and junction site (c).
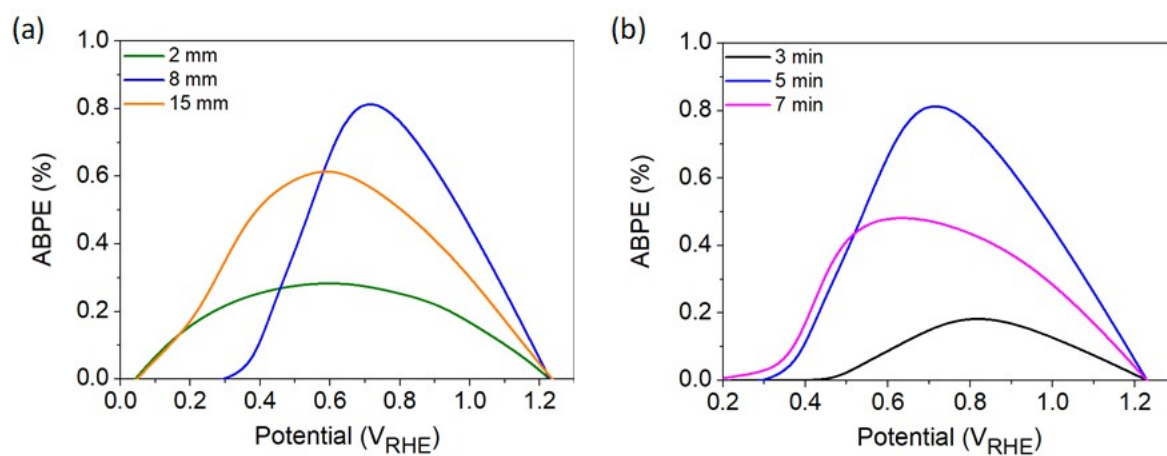
Fig. S12 ABPE curves of TiO_2 prepared at different (a) nozzle-to-FTO distance and (b) deposition time.
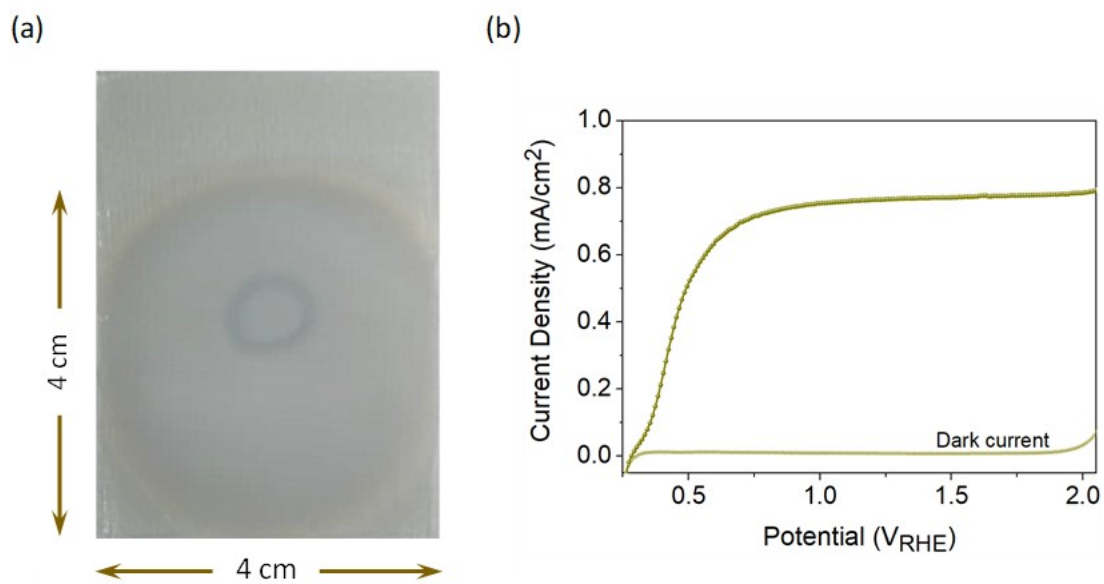
Fig. S13 (a) Photo of TiO_2 film deposited on large substrate (4 cm × 4 cm) and (b) the generated photocurrent density.

Table S1. Mass fraction of anatase and rutile phases in TiO$_2$ films deposited at different temperature.

Deposition Temperature (°C)	Anatase (wt%)	Rutile (wt%)
400	100	0
500	76	24
600	72	28

Table S2. Parameters of fitted EIS curves and the free carrier density of TiO$_2$ samples.

Deposition temperature (°C)	Series resistance, R_S (Ω)	Bulk resistance, R_1 (Ω)	Interfacial resistance, R_2 (Ω)	Free carrier density, N_D
400	21.02	59.95	4114	1.66×10^{20}
500	20.26	19.62	1439	9.76×10^{19}
600	19.73	28.64	1973	1.93×10^{19}

For estimating the donor density (N_D) of each TiO$_2$ sample prepared at different temperatures, the following equation is used:

$$N_D = \frac{2}{e \varepsilon \varepsilon_0 A^2} \left[\frac{d\left(\frac{1}{C^2}\right)}{dE} \right]^{-1}$$

(S1)

where e, ε, ε$_0$, A, C, and E represent the charge of an electron, the dielectric constant of TiO$_2$ (ε = 85), the permittivity of vacuum, the TiO$_2$ photoanode area exposed to the electrolyte, the capacitance of the space charge layer and the applied potential, respectively. d(1/C^2)/dE actually represents the slope of the linear part of the curve.

Table S3. Electrical properties of bare FTO annealed at different temperature.

Annealing temperature (°C)	Carrier concentration (cm^{-3})	Sheet resistance (Ω/sq)	Resistivity (Ω cm)	Conductivity (Ω^{-1} cm^{-1})	Mobility (cm^2 V^{-1} s^{-1})
Unannealed	1.3541×10^{21}	7.0442	1.7611×10^{-4}	5.6784×10^{3}	26.177
400	1.3424×10^{21}	7.0565	1.7641×10^{-4}	5.6686×10^{3}	26.359
500	1.3222×10^{21}	7.0984	1.7746×10^{-4}	5.6351×10^{3}	26.604
600	1.1191×10^{21}	7.0996	1.7749×10^{-4}	5.6341×10^{3}	31.427

Table S4. Comparison of the reported synthesis route for preparing TiO$_2$ photoanode for PEC water splitting.

Methods	Chemicals involved	Film morphology	Min. fabrication time	J$_{SC}$	Light Source	Ref.
Atomic layer deposition + hydrothermal	Tetra(dimethylamino)titanium, tetrabutyl titanate, anhydrous citric acid, hydrochloric acid, pure water, DI water	Compact + nanorod	10 h	~0.4 mA/cm^2 at 1.23 V$_{RHE}$	Simulated solar light (100 mW/cm^2)	[1]
Hydrothermal + Branching growth	DI water, hydrochloric acid, tetrabutyl titanate, boric acid, ammonium hexafluoro-titanate	Nanorod + nanobranches	48 h	~2.3 mA/cm^2 at 1.23 V$_{RHE}$	UV-Vis light (without any filter, intensity 100 mW/cm^2, λ< 400 nm, ca. 20%)	[2]
Hydrothermal	Titanium (IV) isopropoxide, hydrochloric acid, DI water, sodium chloride	Nanorod	18.5 h	2.51 mA/cm^2 at 1.23 V$_{RHE}$	Simulated solar light (100 mW/cm^2)	[3]
Hydrothermal + chemical bath deposition + solvothermal	Titanium tetrachloride, hydrochloric acid, DI water, titanium tert-n-butoxide, sodium chloride, titanium tert-isopropoxide, 1-butanol, acetic acid	Nanodendrite	34 h	2.08 mA/cm^2 at 1.23 V$_{RHE}$	Simulated solar light (100 mW/cm^2)	[4]
Anodization on Ti foil	Glycerol, ammonium fluoride	Nanorod	6 h	0.07 mA/cm^2 at 0 V$_{SCE}$	UV-LED (λ 370 nm, intensity 0.3 mW/cm^2)	[5]
Atmospheric-pressure chemical vapor deposition	Titanium tetrachloride	Bifrustum + Nanoflakes	5 min	2.06 mA/cm^2 at 1.23 V$_{RHE}$	Xenon lamp (100 mW/cm^2)	This work

References

1   F. Cao, J. Xiong, F. Wu, Q. Liu, Z. Shi, Y. Yu, X. Wang and L. Li, *ACS Appl Mater Interfaces*, 2016, **8**, 12239–12245.

2   J. Hu, S. Zhang, Y. Cao, H. Wang, H. Yu and F. Peng, *ACS Sustain Chem Eng*, 2018, **6**, 10823–10832.

3   H. Sutiono, A. M. Tripathi, H. M. Chen, C. H. Chen, W. N. Su, L. Y. Chen, H. Dai and B. J. Hwang, *ACS Sustain Chem Eng*, 2016, **4**, 5963–5971.

4   J. S. Yang, W. P. Liao and J. J. Wu, *ACS Appl Mater Interfaces*, 2013, **5**, 7425–7431.

5   C. Ai, P. Xie, X. Zhang, X. Zheng, J. Li, A. Kafizas and S. Lin, *ACS Sustain Chem Eng*, 2019, **7**, 5274–5282.